Chinese Chemical Letters 36 (2025) 110273

Contents lists available at ScienceDirect

Chinese Chemical Letters

journal homepage: www.elsevier.com/locate/cclet

Rationally constructing metallic Sn-ZnO heterostructure *via in-situ* Mn doping for high-rate Na-ion batteries

Bin Feng[a], Tao Long[a], Ruotong Li[a], Yuan-Li Ding[a,b,*]

[a] College of Materials Science and Engineering, Hunan University, Changsha 410082, China
[b] College of Materials and Chemical Engineering, Key laboratory of Inorganic Nonmetallic Crystalline and Energy Conversion Materials, China Three Gorges University, Yichang 443002, China

ARTICLE INFO

Article history:
Received 9 May 2024
Revised 5 June 2024
Accepted 16 July 2024
Available online 25 July 2024

Keywords:
Mn-doping
Heterostructures
Sodium-ion battery
Sn anode
$Sn\text{-}Zn_{0.9}Mn_{0.1}O$

ABSTRACT

Developing a heterostructure for alloying-based anode for sodium-ion batteries (SIBs) is an efficient solution to accommodate volume change upon sodiation/desodiation and boost sodium storage since it combines the merits of each component. Herein, we report a metallic and microphone-like $Sn\text{-}Zn_{0.9}Mn_{0.1}O$ heterostructure *via* an *in-situ* Mn doping strategy. Based on theoretical calculations and experimental results, the introduction of Mn into ZnO (a small amount of Mn also diffuses into the Sn lattice) can not only enhance intrinsic electronic conductivity but also reduce the Na^+ diffusion barrier inside the Sn phase. When evaluated as anode for SIBs, the obtained heterostructures show a high reversible capacity of 395.1 mAh/g at 0.1 A/g, rate capability of 332 mAh/g at 5 A/g, and capacity retention of almost 100% after 850 cycles at 5 A/g, indicating its great potential for high-power application of SIBs.

Sodium-ion batteries (SIBs) have received widespread attention owing to earth-abundant sodium resources, potential cost competitiveness, and eco-friendliness, showing great potential for energy storage systems [1-5]. To date, developing suitable anode materials for SIBs is always a challenge for well-matching various cathode materials including layered transition oxides, polyanionic compounds, and Prussian blue/white cathodes. Hard carbon has been considered one of the most promising anode materials for the commercial application of SIBs. However, hard carbon anode still suffers from the relatively lower reversible capacity of ~300 mAh/g or below, low working voltage (discharge plateau: 0.01–0.1 V), and high manufacturing cost owing to high annealing temperature (>1000 °C), which is not beneficial for fast charging capability and low-cost applications of SIBs.

Tin (Sn) anode has received widespread interests for SIBs due to its high theoretical capacity of 847 mAh/g and relatively high operating voltage (0.1–0.4 V), ensuring safety upon fast charging [6]. However, large volume change (260%–420%) caused by Sn-based anode during sodium alloying/dealloying processes results in structural destruction and capacity degradation, seriously limiting its practical applications. Researchers have proposed various strategies to address the above issues, such as nanostructures [7-9], porous structures [10-12], and hollow structures [12-15]. Nonetheless, certain hollow structure designs may sacrifice volumetric specific capacity [16]. While reducing nanostructure size can minimize volume expansion, the high specific surface energy of nanostructures can promote self-agglomeration, significantly decreasing the active material utilization over cycling [17].

Constructing heterojunctions is an efficient strategy to boost electron and ion transportation kinetics and structural stability for SIBs [18]. For instance, Guo *et al.* [19] created a MoS_2-$ZnIn_2S_4$ heterojunction to enhance the electrochemical properties of MoS_2. Owing to the synergistic effect between MoS_2 and $ZnIn_2S_4$, the resulting heterojunction establishes a built-in electric field that drives electron transfer, facilitating the electrochemical reaction process. In the case of the alloy anode, Qian *et al.* [20] proposed $Sn/FeSn_2$ heterojunction to mitigate volume expansion in the Sn anode and enhance electron conduction through the $FeSn_2$ layer, significantly improving cycle stability and rate performance. However, both Sn and $FeSn_2$ in this heterojunction are electrochemically active and suffer from significant volume strains during sodium alloying and dealloying reactions, which is probably hard to ensure good interconnection. In this regard, developing a Sn-based heterostructure with an inactive phase would be preferable for offering higher structural integrity. In this work, we choose ZnO as the inactive phase and Sn as the active phase for constructing the Sn-ZnO heterostructure. Owing to the semiconductive nature of ZnO, the charge transportation would be inevitably limited between Sn and ZnO. Thus, regulating electronic structure of ZnO

* Corresponding author.
E-mail address: ylding@hnu.edu.cn (Y.-L. Ding).

https://doi.org/10.1016/j.cclet.2024.110273
1001-8417/

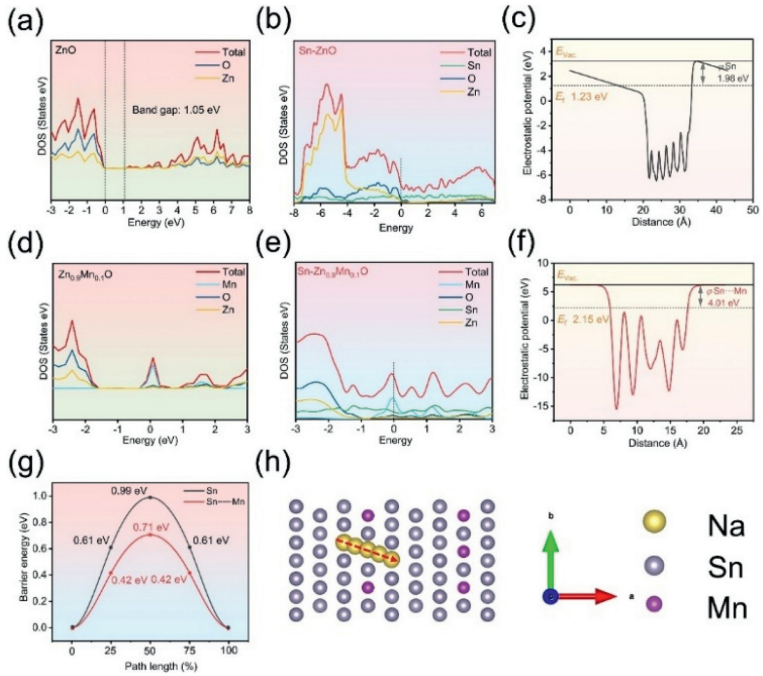

Fig. 1. DOS values of (a) ZnO, (b) Sn-ZnO, (d) $Zn_{0.9}Mn_{0.1}O$, and (e) Sn-$Zn_{0.9}Mn_{0.1}O$. Electrostatic potentials of (c) Sn and (f) Sn···Mn. (g) Na^+ diffusion energy barrier of Sn and Sn···Mn. (h) Diffusion path of Na^+ in Sn···Mn.

would be highly desirable for facilitating electron and ion transfer at the interface of the Sn-ZnO heterostructure.

Herein, we report a facile co-precipitation and subsequent annealing strategy to construct microphone-like and metallic Sn-$Zn_{1-x}Mn_xO$/carbon nanotubes (CNT) heterostructure. In this contribution, the introduction of Mn into ZnO can efficiently regulate the electronic structure of ZnO, realizing metallic characteristics [21], and leading to alterations in electron distribution and Na^+ diffusion pathways across the heterojunction. This adjustment reduces the energy barrier for Na^+ diffusion, ultimately enhancing sodium storage capability of Sn. Furthermore, Mn doping reduces the occurrence of stacking faults in the Sn-ZnO heterojunction, decreases interface surface area, and mitigates charge transport resistance at the heterojunction interface. The as-prepared Sn-$Zn_{0.9}Mn_{0.1}O$/CNT heterostructure material demonstrates a reversible capacity of 371.2 mAh/g at a current density of 1 A/g and maintains a high reversible capacity of 328.6 mAh/g even at a high current density of 5 A/g. When a sodium-ion full cell was assembled with Sn-$Zn_{0.9}Mn_{0.1}O$/CNT negative electrode and $Na_3V_2(PO_4)_3$ (NVP) positive electrode, the device exhibited a reversible capacity of 152.2 mAh/g at 2 A/g.

Density functional theory (DFT) calculations were performed to investigate the electronic properties and structure of Sn-$Zn_{0.1}Mn_{0.9}O$ and understand the effect of Mn doping on its electrochemical properties. The lattice parameters of Sn and ZnO differ significantly, resulting in the formation of a heterojunction interface. Mn-doped ZnO also alters the electronic structure and properties of the heterojunction between Sn and $Zn_{0.9}Mn_{0.1}O$. The total density of states (Total DOS) and partial density of states (DOS) were compared with ZnO (Fig. 1a), Sn-ZnO heterojunction (Fig. 1b), $Zn_{0.9}Mn_{0.1}O$ (Fig. 1d), and Sn-$Zn_{0.9}Mn_{0.1}O$ heterojunction (Fig. 1e). The band gap of ZnO is 1.05 eV, indicating its semiconductor property. Mn doping leads to the formation of metallic $Zn_{0.9}Mn_{0.1}O$, demonstrating the significant enhancement of electronic conductivity. Moreover, both Sn-ZnO and Sn-$Zn_{0.9}Mn_{0.1}O$ heterojunctions exhibit strong metallic properties due to the presence of Sn. Mn doping further increases the electronic conductivity of Sn-ZnO heterojunctions, which is favorable for high-rate charge and discharge processes. According to the calculated work functions, as shown in Figs. 1c and f, the value of Sn in Sn-ZnO (1.98 eV) is lower than the value of Sn in Sn-$Zn_{0.9}Mn_{0.1}O$ (4.01 eV). This indicates that during the charge and discharge process, it is more difficult for electrons to escape from the Sn···Mn (Sn···Mn represents Sn in Sn-$Zn_{0.9}Mn_{0.1}O$/CNT, indicating that a very small amount of Mn has entered into Sn) surface. It suggests that the stability of Sn in Sn-$Zn_{0.9}Mn_{0.1}O$ is enhanced after Mn was doped ZnO. The work functions of ZnO and $Zn_{0.9}Mn_{0.1}O$ are shown in Figs. S2a and b (Supporting information), respectively, with values of 9.04 eV and 6.12 eV. This reveals that it becomes easier for electrons to escape from the ZnO surface after Mn doping, which is well matched with the results of DOS calculations. Such findings show that Mn doping can improve electronic conductivity of ZnO. It is important to note that although it is more difficult for electrons to escape from the Sn surface after Mn doping, the value of the work function of Sn-$Zn_{0.9}Mn_{0.1}O$ (4.01 eV, Fig. S1b in Supporting information) is smaller than Sn-ZnO (6.84 eV, Fig. S1a in Supporting information) when considering the entire heterojunction as the electrode material. This means that electrons are easier to escape from the Sn-$Zn_{0.9}Mn_{0.1}O$ electrode, which will significantly improve its rate capability. In Fig. 1g, the diffusion energy barriers of Na^+ in Sn and Sn···Mn are calculated, respectively. The results demonstrate that Na^+ on the Sn···Mn surface exhibits the anticipated minimum diffusion energy barrier of 0.71 eV, which is lower than the diffusion energy barrier of Na^+ on the Sn surface of 0.99 eV. These findings imply that Mn doping in such Sn-ZnO heterostructure decreases the diffusion energy barrier of Na^+, facilitating efficient Na^+ diffusion. When Na^+ diffuses inside the Sn crystal, the migration site is from Sn to Sn, as illustrated in Fig. 1h.

The overall synthesis schematic diagram of Sn-$Zn_{0.9}Mn_{0.1}O$/CNT is illustrated in Fig. 2a. In this study, a bi-metal $Zn_{0.9}Mn_{0.1}Sn(OH)_6$ nanocubes were used as a template. Initially, $Zn_{0.9}Mn_{0.1}Sn(OH)_6$ was uniformly mixed with -OH CNTs to create a cross-linked carbon network structure. After annealing, $Zn_{0.9}Mn_{0.1}Sn(OH)_6$ nanocubes were converted into microphone-like Sn-$Zn_{0.9}Mn_{0.1}O$

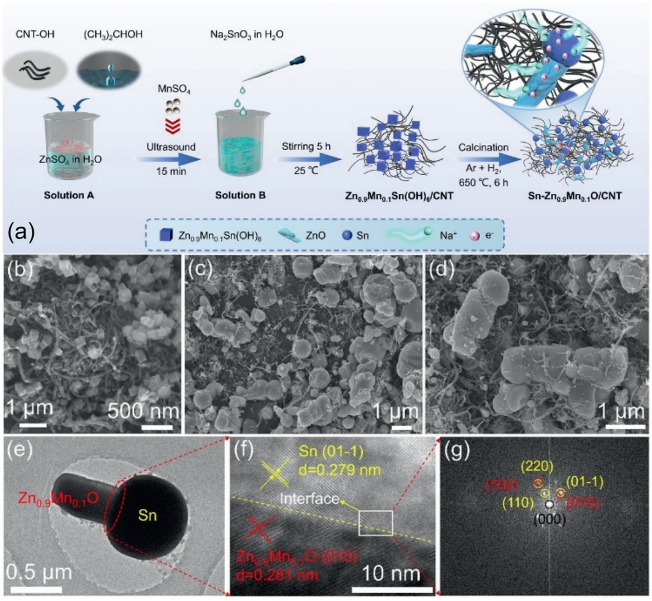

Fig. 2. (a) Schematic illustration of the construction of Sn-$Zn_{0.9}Mn_{0.1}O$/CNT. SEM images of (b) $Zn_{0.9}Mn_{0.1}Sn(OH)_6$/CNT and (c, d) Sn-$Zn_{0.9}Mn_{0.1}O$/CNT. (e) HRTEM images of Sn-$Zn0_{.9}Mn_{0.1}O$/CNT and (f) the TEM morphologies of Sn/$Zn_{0.9}Mn_{0.1}O$ interfacial zone. (g) Fast Fourier transform (FFT) from the marked zone of (f).

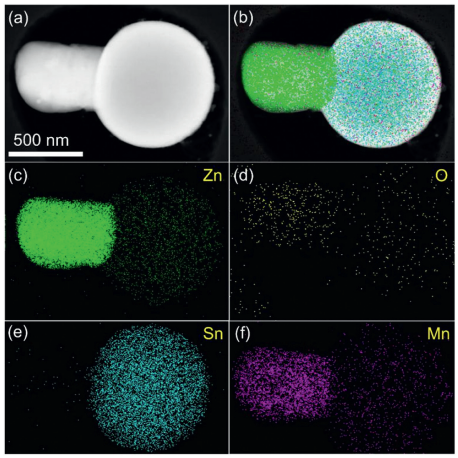

Fig. 3. TEM images of (a) Sn-$Zn_{0.9}Mn_{0.1}O$/CNT and (b) overall element distribution. (c-f) Elemental mapping of Sn-$Zn_{0.9}Mn_{0.1}O$/CNT (Zn, O, Sn, and Mn).

heterostructures with CNTs. For comparison, microphone-like Sn-ZnO heterostructures with CNTs were also prepared by the same synthesis strategy.

As shown in Figs. 2b-f, the microstructure and morphology of $Zn_{0.9}Mn_{0.1}Sn(OH)_6$/CNT were characterized by SEM and TEM. The as-prepared $Zn_{0.9}Mn_{0.1}Sn(OH)_6$ nanocubes are about 200 nm. These nanocubes are cross-linked and entangled with CNTs, as shown in Fig. 2b. $Zn_{0.9}Mn_{0.1}Sn(OH)_6$/CNT is converted to Sn-$Zn_{0.9}Mn_{0.1}O$/CNT heterostructures assembled from rod-shaped $Zn_{0.9}Mn_{0.1}O$ and spheric Sn. Owing to the low melting point of Sn (232 °C), it would escape from $Zn_{0.9}Mn_{0.1}Sn(OH)_6$ nanocubes to generate Sn microspheres at a high-temperature annealing (650 °C). Meanwhile, the rod-like ZnO are also produced due to the pyrolysis of $Zn_{0.9}Mn_{0.1}Sn(OH)_6$ nanocubes. Owing to the synergistical effect of spheric Sn and rod-like ZnO, microphone-like Sn-$Zn_{0.9}Mn_{0.1}O$/CNT heterostructures were formed (Figs. 2c-e). The interface between spherical Sn and rod-like $Zn_{0.9}Mn_{0.1}O$ is identified as the heterojunction interface of Sn-$Zn_{0.9}Mn_{0.1}O$ (highlighted in the red circle area in Fig. 2e).

Compared with $Zn_{0.9}Mn_{0.1}Sn(OH)_6$/CNT and Sn-$Zn_{0.9}Mn_{0.1}O$/CNT, $ZnSn(OH)_6$/CNT and Sn-ZnO/CNT have similar morphology structures, as shown in Figs. S3a-h (Supporting information). To further identify atomic-scale interfacial configuration in the interfacial zones, HRTEM images of Sn/$Zn_{0.9}Mn_{0.1}O$/CNT and Sn-ZnO/CNT interfaces are further presented in Fig. 2f and Fig. S3i (Supporting information). Fig. S3i shows the HRTEM image of the Sn-ZnO/CNT interface, in which the selected zones marked by a box have been further analyzed by fast Fourier transform (FFT), and the corresponding results are displayed in Fig. S3j (Supporting information). It can be identified from FFT that the Sn is a tetragonal structure with unit cell parameters $a = 0.583$ nm, $c = 0.318$ nm (ICDD PDF #04–0673 and the ZnO is a hexagonal structure with unit cell parameters $a = 0.325$ nm, $c = 0.521$ nm (ICDD PDF #36–1451). In addition, it is noted that the hexagonal ZnO plane grows along the $(\bar{1}0\bar{2})$ plane on the Sn $(2\bar{2}0)$ plane, thereby forming the $(\bar{1}0\bar{2})_{ZnO}//(2\bar{2}0)_{Sn}$ nearly coherent interface that ensures the lattice fringes of Sn $(01\bar{1})$ planes almost continuously pass through the lattice fringes of ZnO (010) planes. In a word, there is a high match of interplanar spacing between Sn $(01\bar{1})$ and ZnO (010) planes. The stacking fault will cause interface fracture, lattice distortion, and charge imbalance, which may reduce the electrochemical sodium storage performance [22]. In contrast, there are many stacking faults on the Sn/ZnO interface for Sn-ZnO/CNT heterostructure, leading to large interface surface area and increased charge transfer resistance [23]. As for the Sn-$Zn_{0.9}Mn_{0.1}O$/CNT interface region in Fig. 2f, it is revealed from FFT that the Sn can be identified as the tetragonal structure with (220) planes parallel to Sn/$Zn_{0.9}Mn_{0.1}O$ interface, while $Zn_{0.9}Mn_{0.1}O$ grows along (102) planes. It is noted from FFT in Fig. 2g that the tilted growth leads to the lattice fringes of Sn $(01\bar{1})$ planes nearly continuously passing through lattice fringes of $Zn_{0.9}Mn_{0.1}O$ (010) planes when interplanar spacing of 0.279 nm for Sn $(01\bar{1})$ planes almost same as large as 0.281 nm for ZnO (010) planes. Thus, by doping Mn into Sn-ZnO heterojunction, the number of stacking faults is reduced, which is beneficial to charge transfer.

In addition, elemental mapping was conducted to investigate the distribution of Sn, Zn, O, and Mn (Figs. 3a and b), further confirming microphone-like structure of Sn-$Zn_{0.9}Mn_{0.1}O$/CNT. The rod-shaped part mainly consists of ZnO (Figs. 3c and d), while the spherical part is primarily composed of Sn (Fig. 3e). As shown in Fig. 4a, the thermogravimetric (TG) curves show higher structure stability of the obtained Sn-$Zn_{0.9}Mn_{0.1}O$/CNT than that of Sn-ZnO/CNT. Mn is primarily doped in the Zn position (Fig. 3f), which aligns with the XRD results (Figs. 4b-d). It is worth noting that despite most Mn elements being doped in ZnO, the formation of the Sn-$Zn_{0.9}Mn_{0.1}O$ heterojunction leads to a slight diffusion of phases, resulting in a small amount of Mn entering the Sn regions and altering the crystal structure of Sn. This phenomenon is supported by XRD refinement results (Table S1 in Supporting information) and TG data (Fig. 4e).

The carbon contents of Sn-$Zn_{0.9}Mn_{0.1}O$/CNT and Sn-ZnO/CNT were analyzed using TG analysis (Fig. 4a). The results show that Sn-$Zn_{0.9}Mn_{0.1}O$/CNT has a carbon content of 7.64%, while Sn-ZnO/CNT has a carbon content of 8.85%. The detailed calculation process can be found in Eq. S1 (Supporting information). The phase composition of Sn-$Zn_{0.9}Mn_{0.1}O$/CNT and Sn-ZnO/CNT samples was analyzed by using XRD. Both samples consist of Sn and ZnO phases (Fig. 4b). The synthesized Sn-$Zn_{0.9}Mn_{0.1}O$/CNT and Sn-ZnO/CNT samples match well with Sn (PDF#03–065–2631) and ZnO (PDF#01–070–2551), respectively. From Figs. 4c and d, it can be observed that the position of the Sn phase remains unchanged, while the X-ray diffraction peaks shift to a lower angle by approximately 0.06° after Mn doping in ZnO, indicating an increase in in-

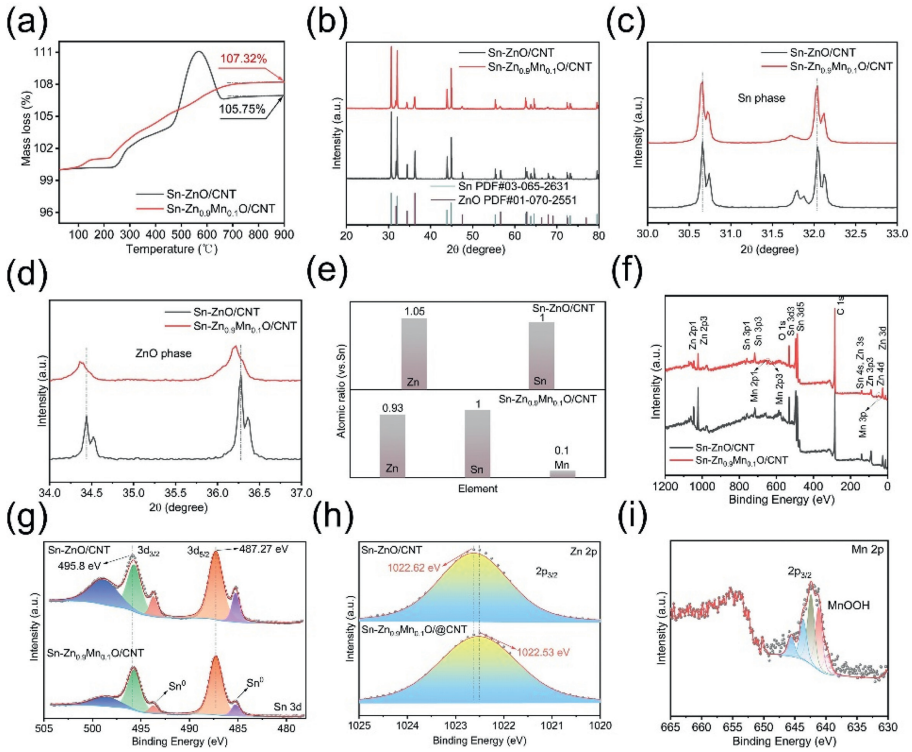

Fig. 4. (a) TGA curves of Sn-$Zn_{0.9}Mn_{0.1}O$/CNT and Sn-ZnO/CNT from 30 °C to 900 °C (air atmosphere). (b) XRD of patterns of Sn-$Zn_{0.9}Mn_{0.1}O$/CNT and Sn-ZnO/CNT. Comparison of XRD diffraction angles of (c) Sn phases and (d) ZnO phases in Sn-$Zn_{0.9}Mn_{0.1}O$/CNT and Sn-ZnO/CNT. (e) ICP results of Sn-$Zn_{0.9}Mn_{0.1}O$/CNT and Sn-ZnO/CNT. (f) XPS survey spectrums of Sn-$Zn_{0.9}Mn_{0.1}O$/CNT and Sn-ZnO/CNT. High-resolution (g) Sn 3d and (h) Mn K-edge XANES and reference samples (Mn foil, Mn_3O_4, MnO, and Mn_2O_3). (i) Zn K-edge XANES (inset: a zoomed-in view) of Sn-$Zn_{0.9}Mn_{0.1}O$/CNT and Sn-ZnO/CNT.

terplanar spacing. The introduction of Mn^{2+} into the ZnO lattice, with a larger radius of 0.83 Å compared to Zn^{2+} (0.74 Å), results in the expansion of the ZnO lattice and an increase in unit cell volume (Table S1).

Figs. S5a and b (Supporting information) depict the refined XRD patterns of Sn-$Zn_{0.9}Mn_{0.1}O$/CNT and Sn-ZnO/CNT, respectively. By analyzing the refined unit cell parameters, it is evident that the unit cell volume of ZnO increases (from 48.060 $Å^3$ to 48.081 $Å^3$), while the unit cell volume of Sn decreases (from 109.09 $Å^3$ to 108.933 $Å^3$, Table S1). These findings indicate that Mn is not only doped into Zn sites but also partially diffuses into the Sn lattice. In addition, the Sn-$Zn_{0.9}Mn_{0.1}O$/CNT and Sn-ZnO/CNT samples were analyzed using ICP elemental analysis (Fig. 4e). The molar ratio of Zn: Mn: Sn in the Sn-$Zn_{0.9}Mn_{0.1}O$/CNT sample was approximately 9:1:10, while the ratio of Zn:Sn in the Sn-ZnO/CNT sample was approximately 1:1. These ratios are well consistent with the designed Zn/Mn ratio in the experiment. As depicted in Fig. 4f, the full survey of XPS spectrums further confirms the presence of Zn, Sn, O, and C in both Sn-$Zn_{0.9}Mn_{0.1}O$/CNT and Sn-ZnO/CNT. It was found that the incorporation of Mn did not have an impact on the chemical state of Sn (Fig. 4g, $3d_{3/2}$ and $3d_{5/2}$ values were both 495.80 and 487.27 eV, with a difference of less than 0.05 eV). The fine electronic structure around Mn (Fig. 4h) and Zn (Fig. 4i) in the resultant samples was probed by X-ray absorption spectroscopy (XAS). In the Mn K-edge X-ray absorption near-edge structure (XANES) spectra, the near-edge absorption of the Sn-$Zn_{0.9}Mn_{0.1}O$/CNT lies lower than Mn_2O_3 but higher than MnO, implying that the average valence state of Mn is between +2 and +3. As illustrated in Fig. 4i, the Zn K-edge XANES spectra shift slightly towards lower energy levels after Mn doping, suggesting a reduction in the valence state of Zn compared to the typical +2 state in ZnO. To further investigate the valence change of Zn, we conducted an analysis of the valence of Zn in both Sn-$Zn_{0.9}Mn_{0.1}O$/CNT and Sn-ZnO/CNT, revealing that the chemical state of Zn (Fig. S6a in Supporting information) did change when Mn was added, as indicated by a decrease in energy from 1022.62 eV to 1022.53 eV, which indicates that the valence state of Zn decreases. The XPS analysis of Mn (Fig. S6b in Supporting information) shows that the average valence state is between +2 and +3, which is consistent with the results of Mn K-edge XANES spectra [24].

To evaluate the effects of Sn-$Zn_{0.9}Mn_{0.1}O$/CNT and Sn-ZnO/CNT on the redox potential and charge/discharge plateaus, we conducted cyclic voltammetry (CV) and galvanostatic charge and discharge (GCD) tests at a scanning rate of 0.1 mV/s. In Figs. 5a and d, the CV curve shows two main redox peaks. These peaks can be attributed to the two-step alloying (C1: $NaSn + 9Na^+ + 9e^- \rightarrow Na_9Sn_4$; C2: $Na_9Sn_4 + 6Na^+ + 6e^- \rightarrow Na_{15}Sn_4$) and the subsequent dealloying process of Sn (A2: $Na_{15}Sn_4 \rightarrow Na_9Sn_4 + 6Na^+ + 6e^-$; A1: $Na_9Sn_4 \rightarrow NaSn + 9Na^+ + 9e^-$) [25]. Although Mn doping did not alter the electrochemical reaction mechanism of Sn anode, we conducted CV test with 0.5 mV/s (Figs. S9a and b in Supporting information) to better elucidate the influence of Mn doping on the electrochemical reaction kinetics. The results revealed that Sn-$Zn_{0.9}Mn_{0.1}O$/CNT exhibited reduced polarization and enhanced response current (Fig. S9c in Supporting information), indicating that the incorporation of Mn can enhance sodium storage reaction kinetics of Sn anode. The GCD curves of Sn-$Zn_{0.9}Mn_{0.1}O$/CNT and Sn-ZnO/CNT at 1 A/g for the 5^{th}, 10^{th}, 30^{th}, 50^{th}, and 100^{th} cycles are displayed in Figs. 5b and e. The decrease in apparent discharge capacity observed in the first cycle is attributed to the formation of the solid electrolyte interphase (SEI) film. The charge-discharge specific capacity of Sn-$Zn_{0.9}Mn_{0.1}O$/CNT (charge: 373.1 mAh/g, discharge: 373.9 mAh/g) is higher than that of Sn-ZnO/CNT (charge: 288.2 mAh/g, discharge: 287.9 mAh/g) at the 100^{th} cycle. The higher capacity values correspond to the phase transformation

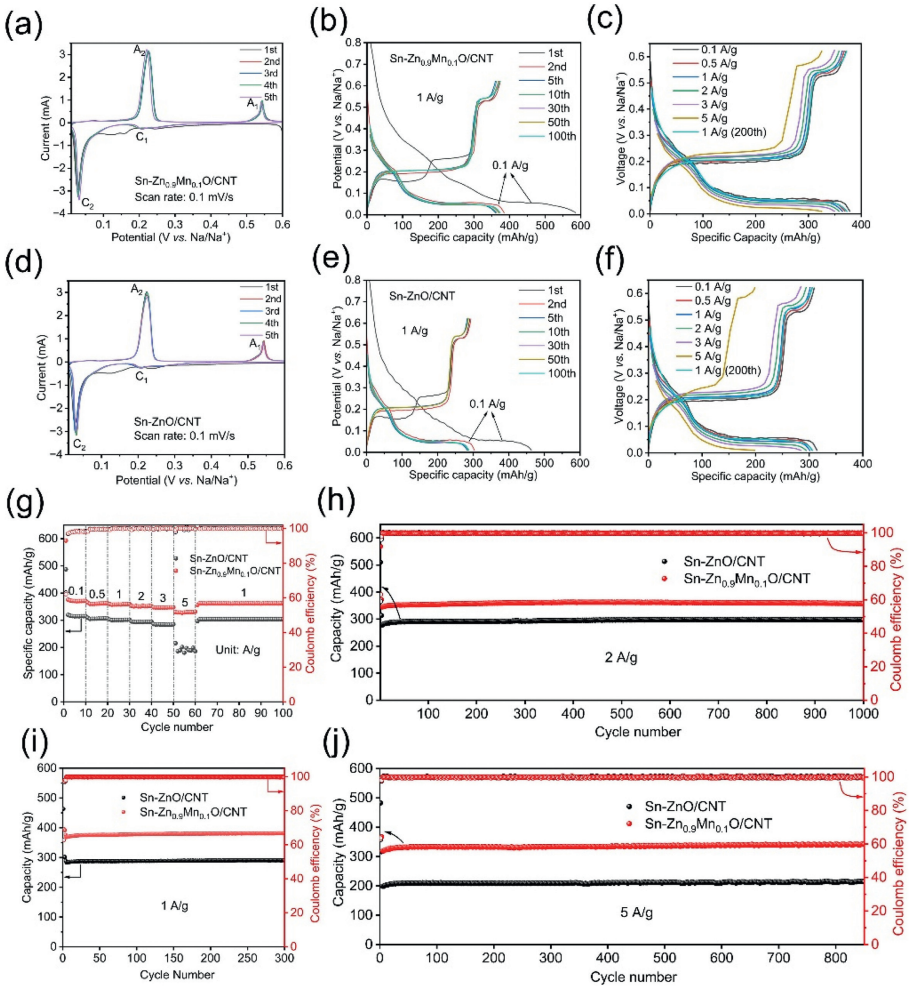

Fig. 5. CV curves of the (a) Sn-$Zn_{0.9}Mn_{0.1}O$/CNT and (d) Sn-ZnO/CNT at a scan rate of 0.1 mV/s. Charge/discharge profiles of (b) Sn-$Zn_{0.9}Mn_{0.1}O$/CNT and (e) Sn-ZnO/CNT electrode at 1 A/g. Charge/discharge profiles of (c) Sn-$Zn_{0.9}Mn_{0.1}O$/CNT and (f) Sn-ZnO/CNT electrodes at different current rates (0.1, 0.5, 1, 2, 3, and 5 A/g). (g) Rate performance of Sn-$Zn_{0.9}Mn_{0.1}O$/CNT and Sn-ZnO/CNT. Cycle performance of Sn-$Zn_{0.9}Mn_{0.1}O$/CNT and Sn-ZnO/CNT electrodes at (h) 2, (i) 1, and (j) 5 A/g.

processes of $Na_9Sn_4 \rightarrow NaSn$ and $Na_9Sn_4 \rightarrow Na_{15}Sn_4$, respectively. This indicates that Mn doping into Sn-ZnO/CNT enhances the reversibility of the alloying/dealloying reaction. To further examine the effect of Mn doping in the obtained heterostructure, rate capabilities were also evaluated for Sn-$Zn_{0.9}Mn_{0.1}O$/CNT and Sn-ZnO/CNT. The evolution of the GCD curves is similar to Fig. 5b, as shown in Figs. 5c and f. Fig. 5g shows that Sn-$Zn_{0.9}Mn_{0.1}O$/CNT provided specific capacity of 378.1, 378.5, 369.2, 364.8, 357.9, and 325.1 mAh/g at 0.1, 0.5, 1, 2, 3, and 5 A/g, much higher than those of Sn-ZnO/CNT (314.6, 305.7, 306.1, 301.4, 294.1, 284.3, and 198.7 mAh/g at 0.1, 0.5, 1, 2, 3, and 5 A/g). Even when the current density returns to 1 A/g, the specific capacity can well return to 371.2 mAh/g. After 1000 cycles at 2.0 A/g, the specific capacity of 357.8 mAh/g can still be maintained, much higher than that of Sn-ZnO/CNT (297.9 mAh/g) (Fig. 5h). Such findings indicate that Sn-$Zn_{0.9}Mn_{0.1}O$/CNT has better rate stability. Furthermore, we compared the specific capacities of Sn-$Zn_{0.9}Mn_{0.1}O$/CNT and Sn-ZnO/CNT after 300 cycles at 1 A/g (Fig. 5i) and 850 cycles at 5 A/g (Fig. 5j), the specific capacities were found to be 381.4 and 341.9 mAh/g, respectively, for Sn-$Zn_{0.9}Mn_{0.1}O$/CNT, and 290.8 and 215.3 mAh/g for Sn-ZnO/CNT. These results further demonstrate high reversible specific capacity and cycle stability of Sn-$Zn_{0.9}Mn_{0.1}O$/CNT at high rates. To investigate the impact of different Mn doping amounts on the electrochemical properties of Sn-$Zn_{1-x}Mn_xO$/CNT heterojunction electrodes, Sn-$Zn_{1-x}Mn_xO$/CNT samples were prepared with Mn doping amounts of 0.05, 0.1, 0.2, and 0.3. In Fig. S7a (Supporting information), it can be observed that Mn doping with various contents does not result in the formation of new phases besides Sn and ZnO. Similar to the case of Sn-$Zn_{0.9}Mn_{0.1}O$/CNT, Mn is predominantly doped at the Zn sites. As shown in Fig. S7c (Supporting information), an increase in Mn doping amount leads to a noticeable shift of XRD diffraction peaks of ZnO towards a lower angle, while XRD diffraction peaks of Sn phase remain relatively unchanged (Fig. S7b in Supporting information). These samples were then tested at 2 A/g (Fig. S10a in Supporting information) and 5 A/g (Fig. S10b in Supporting information) to evaluate their cycle performance. The results showed that the Sn-$Zn_{1-x}Mn_xO$/CNT heterojunction electrode exhibited the highest reversible capacity when the Mn doping amount was 0.1. Both too high and too low Mn doping amounts were found to be detrimental to sodium storage capability of Sn anode. This suggests that excessively low Mn content has minimal impact on the electrochemical behavior of Sn, while excessively high Mn content may impede the diffusion of Na^+ in Sn-$Zn_{1-x}Mn_xO$/CNT.

To investigate the sodium storage behavior of Sn-ZnO/CNT and Sn-$Zn_{0.9}Mn_{0.1}O$/CNT composites, CV measurements were conducted at various scanning rates (0.1–1 mV/s) within a voltage range of 0.01–0.62 V (Figs. 6a and d). As scanning rate increased, the anodic peaks A1 and A2 shifted to higher potential ranges, while the cathodic peaks C1 and C2 shifted to lower potential

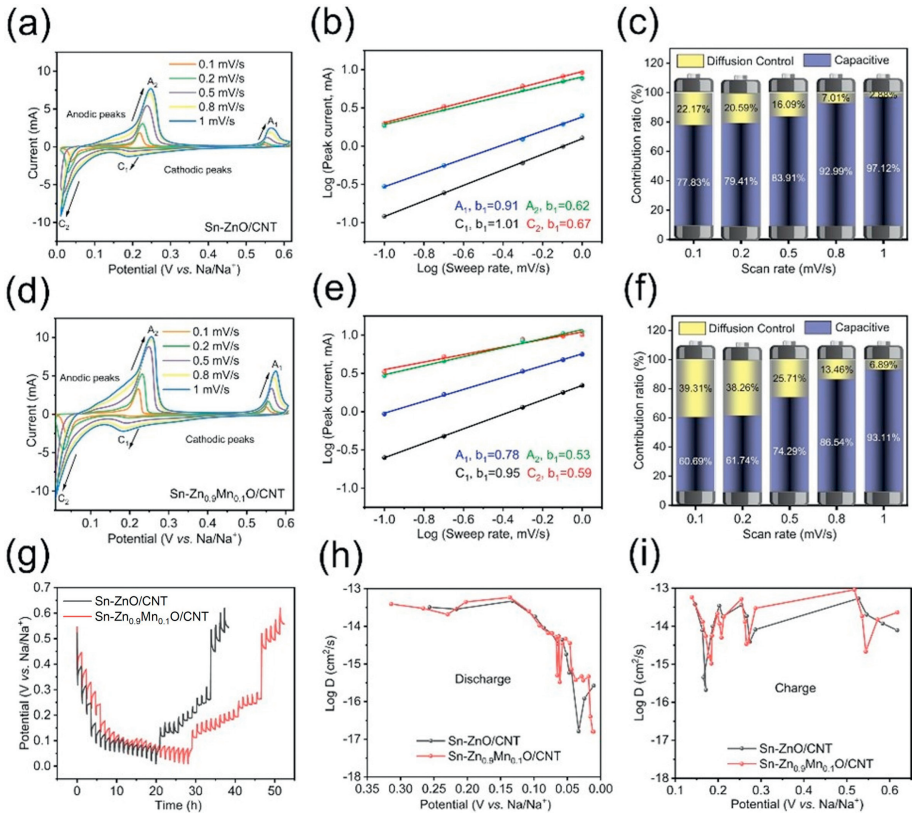

Fig. 6. CV curves of the (a) Sn-ZnO/CNT and (d) Sn-$Zn_{0.9}Mn_{0.1}$O/CNT electrode at various scanning rates from 0.1 mV/s to 1.0 mV/s. Peak current *versus* scan rate for (b) Sn-ZnO/CNT and (e) Sn-$Zn_{0.9}Mn_{0.1}$O/CNT electrodes (logarithmic format). Normalized contribution ratio of capacitive- and diffusion-controlled capacities of (c) Sn-ZnO/CNT and (f) Sn-$Zn_{0.9}Mn_{0.1}$O/CNT at different scanning rates from 0.1 mV/s to 1.0 mV/s. (g) GITT curves and Na^+ diffusion coefficients of Sn-ZnO/CNT and Sn-$Zn_{0.9}Mn_{0.1}$O/CNT during (h) discharging and (i) charging process.

ranges, indicating the presence of surface-induced capacitance behavior. By applying the power law equation that describes the relationship between the current response (i) and the scanning rate (v), we obtained the following transformed equation:

$$i = av^b \tag{1}$$

$$\log(i) = b\log(v) + \log(a) \tag{2}$$

where a is an adjustable parameter, i is the peak current, and v is the corresponding scanning rate. The value of b is determined by the slope factor of the linear fit of $\log(i)$ to $\log(v)$. A b value close to 0.5 indicates a diffusion-controlled process, while a value approaching 1.0 suggests a surface-induced capacitance process. The calculated b values for the anodic and cathodic peaks of Sn-ZnO/CNT and Sn-$Zn_{0.9}Mn_{0.1}$O/CNT (Figs. 6b and e) are 0.91, 0.62, 1.01, and 0.67, and 0.78, 0.53, 0.95, and 0.59 respectively. This indicates that the Na^+ storage behavior of Sn-ZnO/CNT and Sn-$Zn_{0.9}Mn_{0.1}$O/CNT is a combination of diffusion control. Therefore, the contribution of surface-induced capacitance behavior can be further quantitatively distinguished using the following equation:

$$i(\mathrm{V}) = k_1 v^{1/2} + k_2 v \tag{3}$$

$$i(\mathrm{V})/v^{1/2} = k_1 + k_2 v^{1/2} \tag{4}$$

The contributions of the diffusion control process and the surface-induced capacitance process are represented by $k_1 v^{1/2}$ and $k_2 v$ respectively. Fig. 6c illustrates the contribution of the capacitive process at the Sn-ZnO/CNT scanning rates of 0.1, 0.2, 0.5, 0.8, and 1 mV/s (77.83%, 79.41%, 83.91%, 92.99%, and 97.12%, respectively). The contribution is slightly higher than that of Sn-$Zn_{0.9}Mn_{0.1}$O/CNT (Fig. 6f, 60.69%, 61.74%, 74.29%, 86.54%, and 93.1%, respectively). This could be attributed to the enhancement of Sn-$Zn_{0.9}Mn_{0.1}$O/CNT's Faradaic reaction activity due to Mn doping, which reduces the activity of non-electrochemical reactions occurring on the surface. From another perspective, this indicates that Mn doping increases the specific capacity of Sn-$Zn_{0.9}Mn_{0.1}$O/CNT compared to Sn-ZnO/CNT, not by increasing the contribution of surface pseudocapacitance, but by altering the intrinsic structure of the entire composite material. The introduction of Mn into Sn-ZnO/CNT improves electrochemical reaction kinetics, facilitating smooth insertion and extraction process of Na^+ ions. Additionally, it reduces the occurrence of surface non-electrochemical reactions and pseudocapacitance.

The Na^+ diffusion coefficient (D_{Na^+}) of Sn-$Zn_{0.9}Mn_{0.1}$O/CNT and Sn-ZnO/CNT was determined using the galvanostatic intermittent titration technique (GITT). D_{Na^+} can be calculated using Eq. 5 (details are in the experimental section in Supporting information).

$$D = \frac{4}{\pi\tau}\left(\frac{m_B V_M}{M_B S}\right)^2 \left(\frac{\Delta E_s}{\Delta E_\tau}\right)^2 \left(\tau \ll \frac{L^2}{D}\right) \tag{5}$$

In the given equation, τ represents the constant current pulse time (s), m_B denotes the mass (g), V_M indicates the molar volume (cm^3/mol), M_B represents the molar mass (g/mol), and S refers to the gap between the electrode and the electrolyte, which is the contact area (cm^2). ΔE_s represents the steady-state potential change (V) that occurs after passing the current pulse. In contrast, ΔE_τ represents the potential change (V) that occurs after applying a pulse current for a certain pulse time (s) to eliminate the

IR voltage drop (V). As depicted in Fig. 6g, the GITT curves of Sn-$Zn_{0.9}Mn_{0.1}O$/CNT and Sn-ZnO/CNT exhibit similar shapes. However, the Sn-$Zn_{0.9}Mn_{0.1}O$/CNT curve shows a longer charge and discharge plateau. During the alloying process (Fig. 6h), D_{Na^+} of both electrodes initially remained stable (0.6–0.15 V). The Na^+ diffusion coefficients of Sn-ZnO/CNT and Sn-$Zn_{0.9}Mn_{0.1}O$ gradually decrease during the deep alloying reaction (0.15–0.01 V). Firstly, the voltage window of 0.15–0.01 V corresponds to the phase transition process of $Na_9Sn_4 + 6Na^+ + 6e^- \rightarrow Na_{15}Sn_4$, leading to the expansion of the Sn lattice and increasing obstacles to Na^+ diffusion [26]. Secondly, as alloying deepens, the concentration of Na^+ in the material rises, causing mutual repulsion between ions and further limiting diffusion [27]. Lastly, increased alloying results in greater stress and defects in the Sn lattice, potentially trapping or scattering Na^+ [28]. During the dealloying process (Fig. 6i), the obstacles on the diffusion channel are gradually cleared, resulting in a gradual reduction in the diffusion distance of Na^+. Consequently, D_{Na^+} at the charging platform exhibits the opposite pattern to that of the discharge platform. Based on calculations, D_{Na^+} of Sn-$Zn_{0.9}Mn_{0.1}O$/CNT and Sn-ZnO/CNT are between 10^{-13} cm^2/s and 10^{-17} cm^2/s, respectively. The former is higher than the latter, particularly in the deep alloying stage (0.15–0.01 V). This enhancement can be attributed to Mn doping, which optimizes the crystal structure of the heterojunction interface and improves Na^+ diffusion.

To further investigate the charge transfer kinetics, Nyquist plots were obtained for the fresh and cycled states of Sn-$Zn_{0.9}Mn_{0.1}O$/CNT and Sn-ZnO/CNT electrodes. The frequency range of the plots was set from 100 kHz to 0.01 Hz, and the results are presented in Figs. S11a-c (Supporting information). The Nyquist plot consists of a concave semicircle in the high-frequency region, which represents the charge transfer resistance (R_{ct}), and an oblique line in the low-frequency region, which corresponds to the diffusion process of Na^+. The equivalent circuit and electrochemical impedance spectroscopy (EIS) fitting data for Sn-$Zn_{0.9}Mn_{0.1}O$/CNT and Sn-ZnO/CNT electrodes can be found in Fig. S12 and Table S2 (Supporting information), respectively. In a fresh cell, the ohmic resistance (R_s) and charge transfer resistance (R_{ct}) of the Sn-$Zn_{0.9}Mn_{0.1}O$ electrode (Fig. S11a) were approximately 3.68 and 0.52 Ω, respectively. After the activation process (1st cycle), the R_s and R_{ct} values for the Sn-$Zn_{0.9}Mn_{0.1}O$ electrode decreased to 2.76 and 1.3 Ω, respectively, indicating the formation of a stable SEI layer on the electrode material surface. This can be attributed to the good compatibility between Sn-$Zn_{0.9}Mn_{0.1}O$/CNT and 1 mol/L $NaPF_6$ DME electrolyte. Interestingly, the values of R_s and R_{ct} for the Sn-$Zn_{0.9}Mn_{0.1}O$/CNT electrode remained relatively unchanged after the 1st and 100th cycles (Figs. S11b and c in Supporting information). Comparatively, both the Sn-ZnO/CNT electrode and Sn-$Zn_{0.9}Mn_{0.1}O$/CNT electrode exhibit a similar structure. They consistently demonstrate lower R_s and R_{ct} values in fresh batteries and after 1 and 100 cycles, albeit slightly higher than the Sn-$Zn_{0.9}Mn_{0.1}O$/CNT electrode. In conclusion, the properties of the electrolyte/electrode interface have minimal impact on the electrochemical performance of Sn-$Zn_{0.9}Mn_{0.1}O$/CNT.

To investigate effect of Mn doping on the electrochemical Na^+ storage mechanism of the Sn-$Zn_{1-x}Mn_xO$/CNT electrode, we performed an *ex-situ* XRD tests on the Sn-$Zn_{0.9}Mn_{0.1}O$/CNT anode. The potential selection is depicted in Fig. 7a. Figs. 7b and c demonstrate that $Zn_{0.9}Mn_{0.1}O$ remains present throughout the charge and discharge process, while other phases related to ZnO are difficult to detect. This indicates that $Zn_{0.9}Mn_{0.1}O$ is not an active material and the Na_xSn_y intermediate phase consistently exists. Thus, it can be concluded that metal Sn serves as the primary active material for electrochemical sodium storage in the Sn-$Zn_{0.9}Mn_{0.1}O$/CNT electrode. Figs. 7d and e provide enlarged XRD images of Sn-$Zn_{0.9}Mn_{0.1}O$/CNT during the discharging and charging processes, respectively. These images reveal that as the degree of alloying

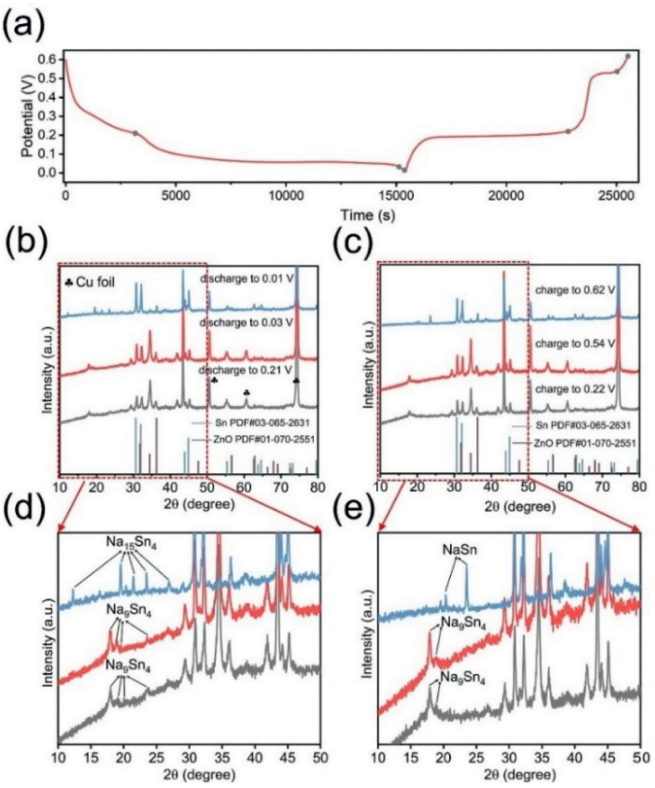

Fig. 7. (a) GCD curve of Sn-$Zn_{0.9}Mn_{0.1}O$/CNT. (b, c) Half-*in-situ* XRD patterns of Sn-$Zn_{0.9}Mn_{0.1}O$/CNT during (b) discharging (0.21, 0.03, and 0.01 V) and (c) charging processes (0.22, 0.54, and 0.62 V) respectively. Partial magnification of XRD patterns of Sn-$Zn_{0.9}Mn_{0.1}O$/CNT during the (d) discharging and (e) charging processes.

deepens, Sn undergoes a transformation from Na_4Sn_9 to Na_4Sn_{15}, and then transitions from Na_4Sn_{15} to Na_4Sn_9 and eventually to NaSn as the degree of dealloying increases. In summary, Mn doping at Zn sites does not influence the electrochemical reaction mechanism of metal Sn.

The performance of the full cell was further evaluated by using Sn-$Zn_{0.9}Mn_{0.1}O$/CNT as anode and $Na_3V_2(PO_4)_3$ (NVP) as cathode (Fig. 8a) [29,30]. Fig. 8b shows that the Sn-$Zn_{0.9}Mn_{0.1}O$/CNT//NVP full cell exhibits two discharge voltage platforms at 3.03 and 2.78 V, which can be attributed to NVP cathode (3.27 V with Na^+/Na) and the voltage difference between the Sn-$Zn_{0.9}Mn_{0.1}O$/CNT anode (0.14 and 0.35 V *vs.* Na^+/Na). The CV curve (Fig. 8c) also reveals the presence of two redox couples in the Sn-$Zn_{0.9}Mn_{0.1}O$/CNT//NVP full cell at 2.78/3.03 V (cathode peak) and 3.3/3.44 V (anode peak). The Sn-$Zn_{0.9}Mn_{0.1}O$/CNT//NVP full cell demonstrates a high discharge specific capacity of 298.4 mAh/g at 0.1 A/g (calculated based on the mass loading of Sn-$Zn_{0.9}Mn_{0.1}O$/CNT). The repeated charge/discharge curve (Fig. 8d) indicates the good cycle performance of the full cell. Even after 60 cycles at 0.5 A/g, it still provides a high capacity of 171 mAh/g, showing good cycle stability (Fig. 8e). Moreover, the Sn-$Zn_{0.9}Mn_{0.1}O$/CNT//NVP full cell exhibits great rate performance, delivering a specific capacity of 152.2 mAh/g even at a high current density of 2 A/g (Fig. 8f). Compared with Sn-ZnO/CNT, Mn doping significantly improves the electrochemical performance of the full cell, as shown in Figs. S13a-c (Supporting information) for details. The electrochemical performance of commercial NVP//Na half cells was also tested, as shown in Figs. S13d–f (Supporting information). Such results show that Sn-$Zn_{0.9}Mn_{0.1}O$/CNT holds promise as a potential anode material for practical applications.

In summary, we have developed Sn-$Zn_{0.9}Mn_{0.1}O$/CNT heterostructure as anode material for SIBs. The synthesis of this mate-

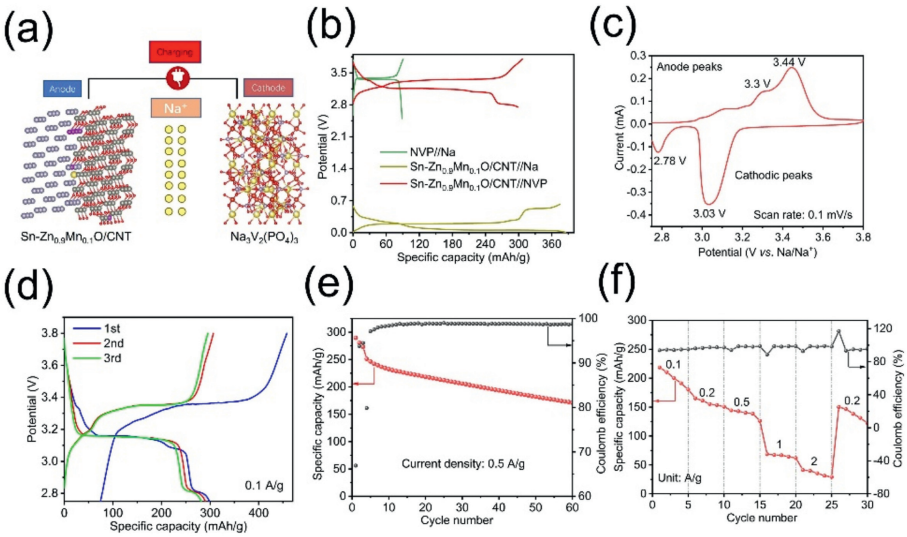

Fig. 8. Electrochemical performance of Sn-$Zn_{0.9}Mn_{0.1}O$/CNT//NVP full cell. (a) Working principle diagram of the full cell. (b) Charge and discharge curves of NVP//Na, Sn-$Zn_{0.9}Mn_{0.1}O$/CNT//Na, and NVP//Sn-$Zn_{0.9}Mn_{0.1}O$/CNT full cells. (c) CV curve of NVP//$Zn_{0.9}Mn_{0.1}O$/CNT full cell at a scan rate of 0.1 mV/s. (d) Charge and discharge curve, (e) cycle performance, and (f) rate performance of NVP//$Zn_{0.9}Mn_{0.1}O$/CNT full cell.

rial involved co-precipitation and high-temperature reduction techniques. The unique interlaced structure of carbon nanotubes and microphone-shaped Sn-$Zn_{0.9}Mn_{0.1}O$ facilitates the transmission of electrons and ions. Theoretical calculations revealed that the Mn-doped heterostructure (Sn-$Zn_{0.9}Mn_{0.1}O$/CNT) exhibited a favorable difference in work function and Fermi level, enhancing electron transfer and improving its performance at high rates. The Sn lattice of Sn-$Zn_{0.9}Mn_{0.1}O$/CNT demonstrated the lowest migration energy barrier for Na^+ ions, indicating an optimal ion transfer path. Additionally, the introduction of Mn reduced the number of stacking faults in the Sn-$Zn_{0.9}Mn_{0.1}O$ heterojunction, leading to a decrease in the interface surface area and promoting charge transport. It is noteworthy that the high-temperature reduction process resulted in trace amounts of Mn diffusing into Sn, which enhanced the thermal stability and conductivity of Sn. When employed as anode for SIB, the obtained Sn-$Zn_{0.9}Mn_{0.1}O$ exhibited excellent rate performance (357.8 mAh/g at 2 A/g and 328.6 mAh/g at 5 A/g) and cycle performance (351.9 mAh/g after 850 cycles at 5 A/g). Compared to undoped Sn-ZnO/CNT, the rate performance of the composite improved by 20.1% (at 2 A/g) and 35.1% (at 5 A/g). The proposed strategy in this work could be extended to the design and synthesis of other alloying anode/metal oxide heterostructures toward high-power battery applications.

Declaration of competing interest

The authors declare that they have no known competing financial interests or personal relationships that could have appeared to influence the work reported in this paper.

CRediT authorship contribution statement

Bin Feng: Writing – review & editing, Writing – original draft, Resources, Methodology, Investigation, Formal analysis, Conceptualization. **Tao Long:** Methodology, Investigation, Formal analysis. **Ruotong Li:** Methodology, Investigation, Formal analysis. **Yuan-Li Ding:** Writing – review & editing, Supervision, Methodology, Conceptualization.

Acknowledgments

This work was financially supported by the National Natural Science Foundation of China (No. 52072119), Hunan Provincial Natural Science Foundation (No. 2023JJ50015), and the 111 Project (No. D20015).

Supplementary materials

Supplementary material associated with this article can be found, in the online version, at doi:10.1016/j.cclet.2024.110273.

References

[1] Y. Fang, L. Xiao, Z. Chen, et al., Electrochem. Energy Rev. 1 (2018) 294–323.
[2] W. Luo, F. Shen, C. Bommier, et al., Acc. Chem. Res. 49 (2016) 231–240.
[3] F. Li, Z. Wei, A. Manthiram, et al., J. Mater. Chem. A 7 (2019) 9406–9431.
[4] H.J. Li, S.C. Han, B.W. Lyu, et al., Chin. Chem. Lett. 32 (2021) 2887–2892.
[5] Y.J. Ke, J.X. Zhang, X. Peng, et al., Nano Res. (2024) 1998-0124.
[6] H. Ying, W.Q. Han, Adv. Sci. 4 (2017) 1700298.
[7] M. Sha, H. Zhang, Y. Nie, et al., J. Mater. Chem. A 5 (2017) 6277–6283.
[8] Y. Liu, N. Zhang, L. Jiao, et al., Adv. Funct. Mater. 25 (2014) 214–220.
[9] H. Wang, E. Matios, C. Wang, et al., J. Mater. Chem. A 7 (2019) 23747–23755.
[10] C. Kim, K.Y. Lee, I. Kim, et al., J. Power Sources 317 (2016) 153–158.
[11] Y. Xu, Y. Zhu, Y. Liu, et al., Adv. Energy Mater. 3 (2012) 128–133.
[12] H. Bian, Z. Li, X. Xiao, et al., Adv. Funct. Mater. 29 (2019) 1901000.
[13] F. He, Q. Xu, B. Zheng, et al., RSC Adv. 10 (2020) 6035–6042.
[14] X. Xiao, W. Yao, T. Yan, et al., Nanoscale 15 (2023) 15405–15414.
[15] W. Zhao, X. Ma, L. Gao, et al., Carbon 167 (2020) 736–745.
[16] L. Yu, X.Y. Yu, X.W. Lou, Adv. Mater. 30 (2018) 1800939.
[17] L. Yu, H. Hu, H.B. Wu, et al., Adv. Mater. 29 (2017) 1604563.
[18] H. Fu, Q. Wen, P.Y. Li, et al., Small Methods 6 (2022) 2201025.
[19] J.Y. Cheng, Z.L. Niu, Z.P. Zhao, et al., Adv. Energy Mater. 13 (2022) 2203248.
[20] M. Chen, P. Xiao, K. Yang, et al., Angew. Chem. Int. Ed. 62 (2023) e202219177.
[21] N. Ali, B. Singh, V.A.R.S. Lal, et al., J. Phys. Chem. C. 125 (2021) 7734–7745.
[22] W. Zeng, W. Shu, J. Zhu, et al., ACS Energy Lett. 9 (2024) 346–354.
[23] M. Han, Z. Liu, X. Shen, et al., Adv. Energy Mater. 10 (2020) 346–354.
[24] M.C. Biesinger, B.P. Payne, A.P. Grosvenor, et al., Appl. Surf. Sci. 257 (2011) 2717–2730.
[25] Y. Zhu, Z. Qian, J. Song, et al., Nano Lett. 21 (2021) 3588–3595.
[26] X.S. Liu, W.H. Zhao, B.Z. Zheng, et al., Angew. Chem. Int. Ed. 134 (2022) e202200475.
[27] Z.Y. Zou, N. Ma, A.P. Wang, et al., Adv. Energy Mater. 10 (2020) 2001486.
[28] N. Kuganathan, N. Kelaidis, A. Chroneos, Materials 12 (2019) 3243.
[29] M. Song, C. Wang, D. Du, et al., Sci. China Chem. 62 (2019) 616–621.
[30] Y. Zhu, Q. Yao, R. Shao, et al., Nano Lett. 22 (2022) 7976–7983.